INTERNATIONAL JOURNAL OF PHYTOREMEDIATION
2026, VOL. 28, NO. 3, 399–411
https://doi.org/10.1080/15226514.2025.2566936

Phytogenic TiO_2–biochar nanocomposite derived from *Prunus dulcis* for enhanced Rhodamine B removal from aqueous systems

James Friday Amaku[a], Ifeoma Anne Omobhude[b], Okoche Kelvin Amadi[c], Tunde Lewis Yusuf[d], Fanyana M. Mtunzi[a], and Jesse Greener[e,f]

[a]Department of Biotechnology and Chemistry, Vaal University of Technology, Vanderbijlpark, Gauteng, South Africa; [b]Department of Pure &Applied Chemistry Faculty of Applied Sciences, Veritas University, Abuja, Nigeria; [c]Department of Chemistry, Michael Okpara University of Agriculture Umudike, Umuahia, Abia State, Nigeria; [d]Department of Chemistry, University of Pretoria, Pretoria, South Africa; [e]Département de Chimie, Université Laval, Québec, QC, Canada; [f]CHU de Québec, Centre de recherche, Université Laval, 10 rue de l'Espinay, Québec, QC, Canada

ABSTRACT

Batch adsorption experiments were carried out to evaluate the removal of Rhodamine B (RhB), a cationic dye, from synthetic wastewater using a multi-walled carbon nanotube/titanium dioxide (MWCNT/TiO_2)-modified biochar composite (CBTM), with pristine biochar (CCB) as a reference. The effects of solution pH, contact time, adsorbent dosage, temperature, and initial dye concentration on adsorption performance were systematically investigated. Maximum RhB removal occurred at pH 3, with equilibrium achieved after 180 min. Under these conditions, CBTM exhibited a higher adsorption capacity (31.43 $mg \cdot g^{-1}$) than CCB (17.31 $mg \cdot g^{-1}$) at 313 K. Equilibrium data were best described by the Freundlich isotherm, indicating multilayer adsorption on heterogeneous surfaces, while kinetic analysis showed that the pseudo-first-order model provided the most accurate fit, suggesting a physisorption-dominated process. Thermodynamic parameters (ΔG°, ΔH°, ΔS°) confirmed that the adsorption was spontaneous and endothermic. Interestingly, while CBTM demonstrated superior dye removal, antimicrobial assays revealed stronger bacterial inhibition by CCB. These results highlight the potential of CBTM for efficient dye removal and underscore the multifunctional capabilities of biochar-based adsorbents.

NOVELTY STATEMENT

This study presents a novel CNT/TiO_2-modified biochar with enhanced dye adsorption capacity and explores its dual functionality by combining adsorption efficiency with antimicrobial activity. The integration of TiO_2 nanomaterials onto biochar for RhB removal represents a promising advancement in multifunctional wastewater treatment materials.

KEYWORDS

Adsorption; antioxidant; biochar; nanocomposite; *Prunus dulcis*; Rhodamine B

Introduction

To attain a state of a healthy and pollutant-free aquatic ecosystem, global environmental policies are periodically modified to accommodate novel contaminants (Reid *et al.* 2019). Hence, amplified consideration has been channeled to environmental contamination in the last 10 years (Morin-Crini *et al.* 2021). Additionally, intensive studies on the evaluation, chemistry, and amount of these contaminants in the waterbodies have been conducted by numerous investigators (Rathi *et al.* 2021). Hence, to mitigate irreversible damage to the ecosystem cycle, it is imperative to sequester or degrade hazardous organic chemicals to less harmful substances in the aquatic ecosystem (Morin-Crini *et al.* 2022).

The release of untreated industrial and domestic wastewater into the water bodies has been identified as the major source of water contamination (Parida *et al.* 2021). Meanwhile, a large fraction of wastewaters reflects the impact of color, suggesting concerns about dye-containing effluent (Al-Tohamy *et al.* 2022). Interestingly, industries such as textiles, medicines, foods, paints, ceramics, pigments, and cosmetics are the major sources of dyestuff in the waterbodies (Samsami *et al.* 2020). About 7×10^5 tons of dyestuff are manufactured yearly, and approximately 15% of these dyes are discharged as effluent (Dutta *et al.* 2022; Shabir *et al.* 2022). Owing to the structural architectures of these dyes, they are robustly stable and resistant to degradation (Waheed *et al.* 2021). As a result, these persistent contaminants remain in industrial effluents, and once discharged, they render water bodies visibly polluted and unappealing (Shabir *et al.* 2022; Khan *et al.* 2023). On the other hand, light penetration into color-imparted waterbodies is impeded, resulting in significant alterations to aquatic ecosystems.

Rhodamine B (RhB) is a water-soluble basic red dye of the xanthene class (Vithalani and Bhatt 2022). It is a reddish violet powder that is significantly used as a water tracer fluorescent (Ratanpara *et al.* 2025). Due to its massive

CONTACT James Friday Amaku fridaya@vut.ac.za Department of Biotechnology and Chemistry, Vaal University of Technology, Vanderbijlpark 1911, Gauteng, South Africa.

application in food and textiles, a study revealed that short exposure to RhB can cause respiratory tract, eyes, and skin irritation (Saravanan *et al.* 2022). Meanwhile, a long-term exposure to RhB may result in persistent toxicity, carcinogenicity, and reproductive impairment (Elliott *et al.* 1990). Various biological and physicochemical treatment techniques have been employed for the elimination of colors from industrial effluents. Wastewater treatment techniques such as adsorption (Mousavi *et al.* 2023), coagulation (Adeogun and Balakrishnan 2017), ion exchanges (Kumar 2019), advanced oxidation processes (Yang *et al.* 2019), biological (Abu Hasan *et al.* 2020), electrochemical approaches (Wu *et al.* 2019), precipitation, and membrane separation (Saleh and Ali 2018) have been significantly established for dye removal from aqueous media. Main drawbacks of the aforementioned techniques include high volume chemical and reagent costs, secondary pollutant generation, easy degradation of the membrane, and complex operation (Saleh *et al.* 2022; Sheng *et al.* 2024).

Adsorption is recognized for its remarkable ability to remove synthetic dyes from wastewater. This method is widely regarded as both technically efficient and economically advantageous, enhancing the overall effectiveness of water treatment processes (Deng *et al.* 2021). Many researchers have reported on the application of adsorption in the removal of dyes (Wang *et al.* 2020; Rathi and Kumar 2021). The efficacy of this technique is attributed to the nature and density of functional groups, the hierarchical pore structure, and the specific surface area of the adsorbent (Demiral *et al.* 2021; Feng *et al.* 2021). Activated carbon has demonstrated superior potential in eliminating a variety of contaminants from wastewater and has gained popularity in the adsorption process (Jjagwe *et al.* 2021; Azam *et al.* 2022). However, a major drawback to the application of activated carbon is its cost of production and poor regeneration characteristics (Saputro *et al.* 2020; Gkika *et al.* 2022).

Hence, stakeholders have garnered greater attention toward the design of readily available and economically viable adsorbents. Literature mining showed that a number of absorbents, including water chestnut peel (Khan *et al.* 2013), red mud (Gupta *et al.* 2004), *Aleurites Moluccana* (Postai *et al.* 2016), composite beads (Hayeeye *et al.* 2017), TiO_2 (Rajeev Jain *et al.* 2007), nanoparticles (Motahari *et al.* 2015), walnut shells (Shah *et al.* 2013) and activated carbon (Mousavi *et al.* 2023) amongst others, have been employed for the elimination of RhB.

Biochar (BC) is a solid with a high carbon content that is produced by pyrolyzing biomass at high temperatures in a limited oxygen supply (Bella and Bendaikha 2022; Qin *et al.* 2022). Owing to its advantageous properties, including surface modifiability, rapid synthesis, facile regeneration, and biocompatibility, biochar has found extensive applications across various industrial processes (Yang *et al.* 2020). Biochar has demonstrated excellent capacity for the removal of toxic pollutants *via* the adsorption technique (Ambaye *et al.* 2021). *Prunus dulcis* nuts are known for their massive health benefits. *Rosaceae, Prunus, and Plantae* are the Family, Genus, and Kingdom of the *Prunus dulcis* plant (Gupta *et al.* 2020; Khalid *et al.* 2021). The nuts of *Prunus dulcis* are rich in calcium and phosphorus, which are essential for the wellness of bone health (Levent 2022). The nutshells of *Prunus dulcis* litter the environment after deshelling. On the contrary, *Prunus dulcis* nutshells exhibit good structural architecture that is beneficial for the fabrication of biochar (Shaikhiev *et al.* 2021). Therefore, producing biochar from *Prunus dulcis* nutshells for environmental remediation not only valorizes this biomass but also provides a sustainable adsorbent. It is important to note that the source of *Prunus dulcis* nutshells can influence reproducibility, as their chemical composition and structural properties may vary with geographic origin and cultivation conditions. In this study, we characterized the physicochemical properties of the nutshells used, providing a reference for future research. This approach ensures comparability and reliability when using biomass from different regions. Titanium dioxide (TiO_2), characterized by high thermal stability and low toxicity, is widely utilized as an industrial pigment, disinfectant, and photocatalyst. (Arun *et al.* 2023). In environmental remediation practice, TiO_2 has demonstrated excellent performance (Alsheheri 2021; Krakowiak *et al.* 2021). Hence, the fabrication of a composite using biochar and TiO_2 is anticipated to sustain superior trapping capacity with disinfection characteristics.

This study aimed to examine the synergistic effect of synthesized TiO_2-supported *Prunus dulcis* nutshell biochar in the sequestration of RhB using varied adsorptive conditions for the sake of optimizing the uptake process. The investigation further probed into the antioxidants and antibacterial characteristics of the biochar and nanocomposite.

Materials and methods

Butyl titanate ($Ti(OC_4H_9)_4$), sodium chloride, polyethylene glycol, rhodamine B, nitric acid, ethanol, acetic acid, hydrochloric acid, sulfuric acid, sodium hydroxide, and all other analytical reagent (AR) grade chemicals were procured from Sigma-Aldrich and used without further purification. *Prunus dulcis* nutshells, utilized as a precursor material, were obtained from Orieagu Market in Umuakagu-Nsu, located in the Ehime Mbano Local Government Area of Imo State, Nigeria.

Preparation of biomass

Ground *Prunus dulcis* nutshells were used as the biowaste for this process, and they were pyrolyzed for one hour at 450 °C in a tubular furnace with a restricted air supply. The pyrolysis process was followed by thorough washing of the biochar (CCB) using acetone, ethanol, and deionized water, which was then dried in an oven. Finally, the biochar was crushed into fine particles, sieved, and stored for later use.

Nanocomposite fabrication

Under constant stirring (150 rpm) for 30 min, MWCNTs (1 g) were weighed into ethanol (100 cm^3). Thereafter, 50 cm^3 butyl titanate was transferred into the mixture and stirred for a further 30 min to obtain mixture A. A separate

solution (B) consisting of polyethylene glycol (3 cm^3), deionized water (5 cm^3), ethanol (30 cm^3), and acetic acid (15 cm^3) was prepared. The composite was then fabricated from the dropwise addition of solution B into mixture A with continuous stirring for 30 min, and the dark homogeneous sol-gel was then allowed to age for 24 h. About 10 g of CCB was then weighed into the dark homogeneous sol-gel and stirred at 150 rpm for 60 min. The final mixture is allowed to age for 24 h, filtered, dried, and calcined for 60 min at 350 °C to produce the MWCNTs/TiO_2/BC composites (CBTM).

Characterization

Powder X-ray diffraction (XRD) patterns of CBTM and CCB were recorded in the 2θ range of 10–80° using a Bruker D8 Advance diffractometer (Bruker, USA). Fourier transform infrared (FTIR) spectra of CBTM, CBTM-RhB, CCB, and CCB-RhB were obtained with a ThermoFisher Scientific spectrophotometer (Waltham, MA, USA) in ATR mode over the range 4000–400 cm^{-1} at a resolution of 2 cm^{-1}. The surface morphology of the samples was examined using scanning electron microscopy (SEM, JSM-7500F; JEOL, Tokyo, Japan). Thermogravimetric analysis (TGA) was performed to evaluate the thermal stability of the adsorbents under a nitrogen atmosphere, with a heating rate of 10 °C/min, using a PerkinElmer STA6000 simultaneous thermal analyzer (USA). The point of zero charge (pH_pzc) for CBTM and CCB was determined following the procedure outlined by Mondal and Basu (Mondal and Basu 2019).

Antioxidant assay

The antioxidant potential of the synthesized biochar (CCB) and nanocomposites (CBTM) was quantitatively evaluated using the 2,2-diphenyl-1-picrylhydrazyl (DPPH) free radical scavenging assay. This method is based on the reduction of the DPPH radical, a stable free radical characterized by a deep violet color, upon interaction with antioxidant compounds. To perform the assay, a DPPH working solution was first prepared at a concentration of 0.3 mM in methanol. Aliquots of this solution (0.5 cm^3) were then added to 2.5 cm^3 of methanolic suspensions of CCB or CBTM at varying concentrations (25, 50, 100, 200, and 400 g cm^{-3}). These concentrations were chosen to evaluate the dose-dependent radical scavenging behavior of the materials. The mixtures were vortexed gently to ensure homogeneity and subsequently incubated in the dark at a controlled temperature of 25 ± 1 °C for 30 min to prevent photo-degradation of the DPPH radical. The absorbance of each mixture was measured at 517 nm using a UV-Vis spectrophotometer against a methanol blank. A decrease in absorbance at this wavelength indicates the scavenging of DPPH radicals by the test samples (Begum et al. 2022). All measurements were performed in triplicate to ensure the accuracy and reproducibility of the results. The percentage inhibition of DPPH radicals was calculated using Eq. (1).

$$I\% = \frac{\left(Asorbance_{control} - Asorbance_{Sample}\right)}{Asorbance_{control}} \times 100 \quad (1)$$

Antibacterial activity

The antimicrobial efficacy of CCB and CBTM was investigated using the agar-well diffusion technique. This assay was designed to evaluate the inhibitory effects of the materials against selected pathogenic bacteria, specifically *Staphylococcus aureus* (Gram-positive) and *Escherichia coli* (Gram-negative). Ciprofloxacin, a broad-spectrum antibiotic, was used as the positive control to validate the assay. Bacterial cultures were first prepared by inoculating standard strains of *S. aureus and E. coli* into sterile nutrient broth, followed by incubation at 37 ± 1 °C for 18–24 h to attain active growth phases. The microbial suspensions were subsequently standardized to match the 0.5 McFarland turbidity standard, ensuring uniformity in bacterial load across all test plates. Sterile Petri dishes containing solidified Mueller-Hinton Agar (MHA) were uniformly seeded with the bacterial suspensions using sterile cotton swabs to ensure a confluent lawn of microbial growth. Wells approximately 10 mm in diameter were carefully bored into the agar using a sterile cork borer. Into each well, 250 µg of either CBTM or CCB sample, prepared in sterile distilled water, was introduced. Control wells containing ciprofloxacin (5 µg per well) served as positive references for antimicrobial activity. The inoculated plates were incubated at 37 ± 1 °C for 24 h under aerobic conditions. Post incubation, the antimicrobial activity was determined by measuring the diameter of the clear zones (zones of inhibition (ZOI)) formed around each well using a digital caliper. The size of these zones indicated the extent of bacterial growth suppression and was directly correlated with the antimicrobial potential of the test samples. All tests were carried out in triplicate to ensure statistical reliability, and the results were expressed as mean values with standard deviations (Qamar et al. 2017).

Sorption experiments of RhB on CBTM and CCB

The adsorption of RhB onto CBTM and CCB was evaluated using 100 mg·dm^{-3} RhB solutions (25 cm^3) with 0.05 g of CBTM and CCB placed in stoppered amber glass bottles and agitated in a thermostatic shaker at 150 rpm for specified time intervals. The effect of solution pH on RhB adsorption was examined by varying the initial pH from 2.0 to 12, using an initial RhB concentration of 100 mg·dm^{-3}, an adsorbent dose of 0.03 g, a temperature of 25 °C, and a contact time of 180 min. pH adjustments were made with 0.1 M NaOH and 0.1 M HCl solutions. The optimum pH identified from this study was used for subsequent experiments. Equilibrium adsorption studies were conducted over a RhB concentration range of 10 to 100 mg·dm^{-3}, with an adsorbent dose of 0.03 g, initial pH of 3, and a 180-minute agitation period at room temperature. Adsorption kinetics were investigated at an initial RhB concentration of 100 mg·dm^{-3}, 0.03 g adsorbent, pH 3, and contact times ranging from 5 to 180 min at 25 °C. After the adsorption period, the

suspensions were filtered, and the residual RhB concentrations were quantified using a UV–Visible spectrophotometer (Shimadzu UV-3600) at a wavelength of 650 nm. All experiments were carried out twice. Eqs. (2) and (3) were used to determine the adsorption capacity (mg g^{-1}) and adsorption efficiency (% adsorbed) of CBTM and CCB, respectively:

$$q_{eq} = \left(\frac{C_i - C_{eq}}{m} \right) V \tag{2}$$

$$\%\ adsorbed = \left(\frac{C_i - C_{eq}}{C_i} \right) \times 100 \tag{3}$$

where V is the volume of the adsorbate. C_i is the initial adsorbate concentration (mg dm^{-3}), C_{eq} is the equilibrium concentration (mg dm^{-3}) of the adsorbate after adsorption, and m is the mass (g) of CBTM or CCB. Models of intraparticle diffusion, pseudo-second order, pseudo-first order, and Elovich kinetics were used to fit experimental data from the contact time experiments into non-linear kinetic models (see Table 1). To ascertain the efficacy and mechanism underlying RhB adsorption onto CBTM and CCB, the Freundlich and Langmuir isotherms were used to analyze the isotherm data (see Table 2).

Data analysis

Nonlinear regression analysis was performed using the NLS (Nonlinear Least Squares) function within the R statistical computing environment to fit the experimental data obtained from the temperature, concentration, and time-dependent studies to their respective kinetic models. This approach enabled the estimation of model parameters by minimizing the residual sum of squares between the observed data and the predicted values, thereby facilitating a robust evaluation of the underlying mechanisms governing the system behavior. The suitability and reliability of the models employed in this study were assessed by calculating the sum of squared residuals (SSR). This statistical metric quantifies the discrepancy between observed and predicted values, serving as an indicator of the model's goodness-of-fit. A lower SSR value signifies a better model performance, reflecting minimal deviation of the model predictions from the experimental data.

Table 1. Kinetics models used to assess the uptake of RhB onto CBTM and CCB.

Kinetic models	Equations	Parameters	References
Pseudo-first order	$\frac{dq_t}{d_t} = k_1(q_e - q_t)$	q_e, k_1	(Aksu & Karabayır, 2008)
Pseudo-second order	$\frac{dq_t}{d_t} = k_2(q_e - q_t)^2$	k_2, q_e	(Sevim et al., 2011)
Weber-Morris intraparticle diffusion	$\frac{dq_t}{d_{t^{-0.5}}} = k_{id}$	k_{id}, I	(Ofomaja et al., 2009)
Elovich	$\frac{dq_t}{d_t} = \alpha exp(-\beta q_t)$	α, β	(Omorogie et al., 2016)

α, adsorption rate constant (mg $g^{-1}min^{-1}$); k_1, pseudo-first order rate constant (min^{-1});. k_{id}, intraparticle diffusion rate constant (mg g^{-1} $min^{0.5}$); q_e, quantity of adsorbate adsorbed at equilibrium (mg g^{-1}); I, is a constant related to the boundary layer thickness (mg g^{-1}); k_2, pseudo-second order rate constant (g $mg^{-1}min^{-1}$) q_t, quantity of adsorbate adsorbed at time t (mg g^{-1}); β, desorption rate constant (g mg^{-1}).

Results and discussions

This section presents a comprehensive characterization of the synthesized biochar and its nanocomposite, focusing on their structural, morphological, and surface properties. It further details the outcomes of batch adsorption experiments conducted to optimize key operational parameters influencing the materials' adsorption efficiency. Beyond their performance as adsorbents, the biochar and nanocomposite were also assessed for their antioxidant and antimicrobial properties, highlighting their potential for multifunctional applications. Additionally, the reusability and long-term stability of the adsorbents were investigated through multiple adsorption–desorption cycles, providing insight into their practical viability for sustainable environmental remediation.

Surface morphology

Figure 1 shows the SEM micrograph of CCB, CCB-RhB, CBTM, and CBTM-RhB. The walls of the biochar (CCB) appear smooth with isolated pores distributed on it, suggesting complete carbonization. After the adsorption of RhB, however, the carbonization is broken down, as seen in the rough surfaces of the CCB-RhB micrograph. The CBTM micrograph shows the intertwined, tubular, fibrous structures of MWCNTs embedded on the biochar surface. Aggregation due to pore blockage by RhB on the CBTM surface is observed on the CBTM-RhB micrograph.

FTIR analysis

FTIR analysis of CBTM and CCB was carried out to characterize the functional groups present in these adsorbents. The FTIR spectra of CBTM, CBTM-RhB, CCB, and CCB-RhB are presented in Figure 2. The broad absorption band observed at approximately 3,473 cm^{-1} is associated with O–H stretching vibrations, indicative of hydroxyl groups in phenolic compounds and hydrogen-bonded water molecules. The band at about 2855 cm^{-1} in CCB and CCB-Rh is associated with the weak C–H stretch of aliphatic groups, which shifts to approximately 2900 cm^{-1} in CBTM and CBTM-Rh, possibly as a result of MWCNT and TiO_2 incorporation. In the

Table 2. Isotherm equations and parameters used to describe the uptake of RhB onto CBTM and CCB.

Isotherm model	Equation	Parameters	References
Langmuir	$q_e = \frac{q_{max} b C_e}{1 + bC_e}$	q_{max}, b	(Langmuir, 1918)
Freundlich	$q_e = K_F C_e^{1/n}$	k_F, n	(HMF Freundlich 1906)

q_{eq}, adsorption capacity (mg g^{-1}) of CBTM and CCB; C_{eq}, equilibrium concentration of RhB in solution (mg dm^{-3}); q_{max}, maximum monolayer potential (mg g^{-1}) of CBTM and CCB; b, Langmuir isotherm constant (dm^3 mg^{-1}); K_F, Freundlich isotherm constant (mg g^{-1}) ($dm^{-3}mg^{-1}$) n, adsorption intensity.

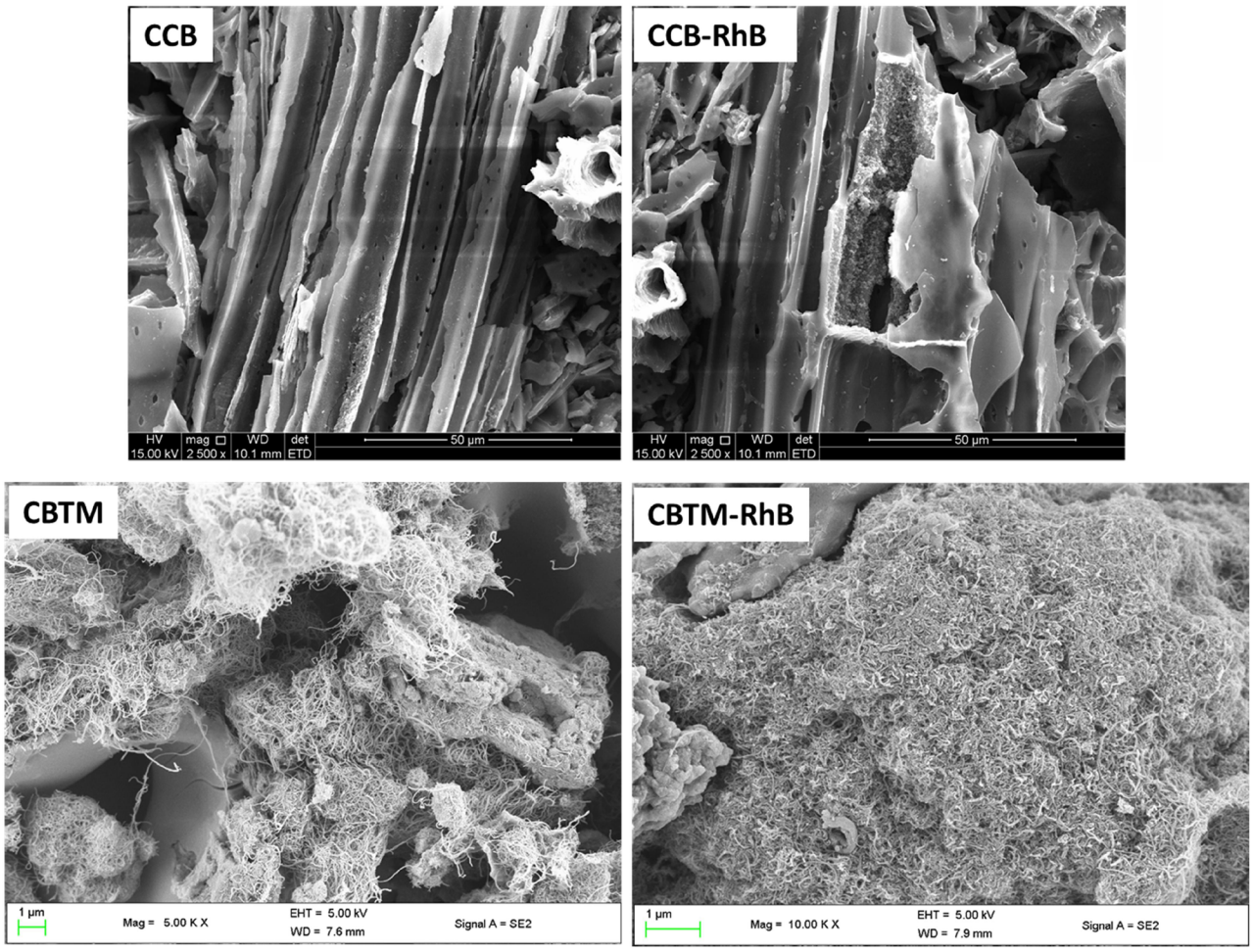

Figure 1. SEM micrographs of CCB, CCB-RhB, CBTM, and CBTM-RhB.

CBTM and CBTM-Rh spectra, the peaks at approximately 1637 cm^{-1} are due to Ti-OH stretching (L. S. Chougala *et al.* 2017). The peak at approximately 1560 cm^{-1} may be attributed to a C=C stretching vibration caused by the aromatic structure, which has higher intensity for CBTM and CBTM-Rh due to the incorporation of MWCNTs. Phenolic and carboxylic groups are responsible for the peaks at approximately 1440 cm^{-1}. The high intensity peaks at around 1000 cm^{-1} for CCB and CCB-Rh are attributed to the –C–O–C– stretching vibrations of polysaccharides or the bending vibrations of –C–OH (Firet and Smith 2017; Smith 2017). The intensity of this peak decreases in the nanocomposite due to the incorporation of MWCNTs and TiO_2. The CBTM and CBTM-Rh spectra show strong peaks of Ti–O–Ti lattice vibrations at approximately 489 $cm^{-1,}$ confirming the presence of titanium dioxide in the nanocomposite (Raguram and Rajni 2022).

Thermogravimetric analysis

The thermograms from thermogravimetric analysis are presented in Figure 3. Both thermograms showed decomposition at 30–105 °C due to moisture loss. The mass losses at 350 °C and 300 °C on the CCB and CBTM thermograms are associated with the hemicellulose and cellulose content of the biochar. Approximately 18% weight of the remaining biochar in CCB is attributed to residual ash minerals. In the CBTM thermogram, about 40% remaining weight is associated with TiO_2 due to the incombustible metal oxide.

Phase analysis

The XRD patterns of the CCB biochar and CBTM nanocomposite are shown in Figure 4. The biochar prepared by conventional pyrolysis shows distinct peaks at 25.5° and 40.7°. The 25.5° peak is commonly associated with the (002) plane of graphitic carbon. It indicates the presence of ordered carbon structures, which might result from the pyrolysis process during biochar production (Liu *et al.* 2018; Yoo *et al.* 2018). The other peak at 40.7° corresponds to the (100) or (101) planes of hexagonal graphite or other crystalline phases. It may also indicate the presence of minerals or inorganic compounds derived from the plant material. CBTM XRD pattern shows peaks at 25.7°. This corresponds to the primary (002) reflection of turbostratic/graphitic carbon, which is common in biochar and MWCNTs (Jafari *et al.* 2012; Yan *et al.* 2024). The slight shift from ideal graphite (26.5°) could be due to disorder, defects, or oxygen functional groups. The higher intensity of the peak is typically due to MWCNTs and TiO_2 (anatase) compared with biochar alone. The peaks 38.4°, 48.4°, 54.4°, 55.7°, 63.4°, 69.3 70.9°, and 75.5° are associated to the planes (004), (200), (105), (211), (204), (116), (220), and (215) respectively and are characteristics of anatase TiO_2 (JCPDS card no. 21–1272) (L. Chougala *et al.* 2017).

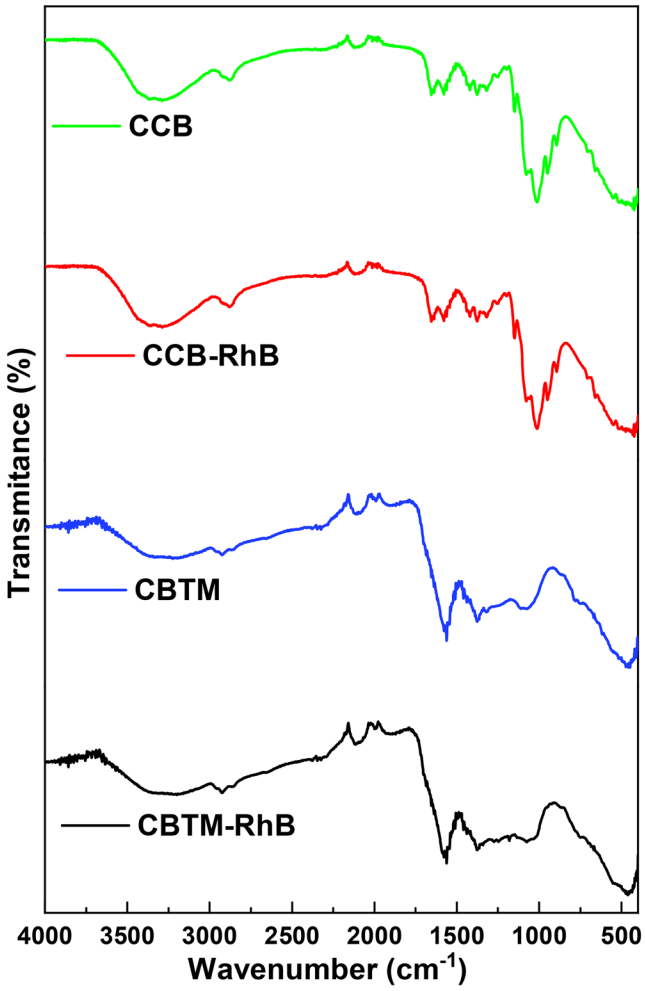

Figure 2. FTIR spectra of CBTM, CBTM-RhB, CCB, and CCB-RhB.

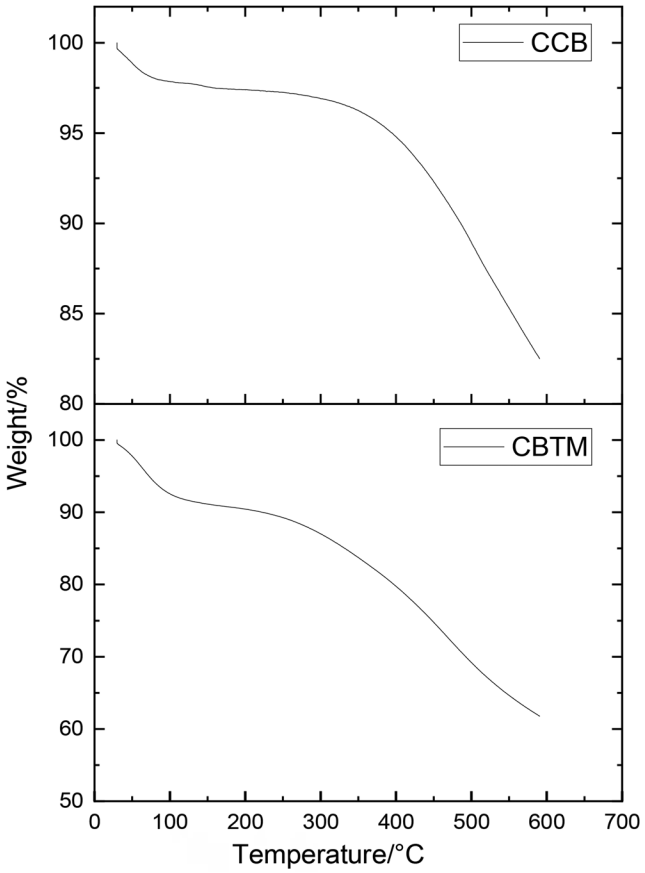

Figure 3. The TGA thermograms of CBTM and CCB.

Sorption experiments

This section highlights the optimization of Rhodamine B adsorption onto CCB and CBTM, taking into account key adsorption parameters such as pH, adsorbent dosage, solution temperature, and contact time. It also evaluates the reusability of the adsorbents, along with their antioxidant and antimicrobial properties, to assess their overall effectiveness as water treatment agents.

The effect of pH

The surface of CCB and CBTM exhibited a pH_{PZC} of 5.68 and 5.01, respectively (see Figure 5). This shows that at pH values greater and lesser than these values, the surface of the adsorbents will be negatively and positively charged, respectively. From the graph depicted below (see Figure 6), which elucidates the relationship between the adsorption capacity of CCB and CBTM and the initial solution pH of Rhodamine B. The adsorption capacity of CBTM exhibited a gradual increase from 25 $mg{\cdot}g^{-1}$ to 33 $mg{\cdot}g^{-1}$ as the solution pH rose from 1 to 3. Similarly, the uptake capacity of CCB increased from 12.5 $mg{\cdot}g^{-1}$ to 17.5 $mg{\cdot}g^{-1}$ within the same pH range. However, beyond this optimal pH value, a noticeable decrease in the adsorption performance of both CBTM and CCB was recorded. The observed phenomenon may be attributed to the cationic nature of rhodamine B, which forms monomeric molecules that are smaller in size. The reduced sizes of these molecules enable them to enter the pores of the CCB and CBTM. On the other hand, a reduction in the trapping capacity of the adsorbent was observed as the pH increased above 3. This may be due to the increasing formation zwitterionic form of rhodamine B with increased pH. The higher the amount of zwitterions formed, the greater the tendency for the formation of dimers. The dimers are bigger molecules that find it difficult to attach themselves to the pores of the adsorbent. Hence, a size-dependent screening effect is observed with increased solution pH. From the result, the adsorption of rhodamine B by CCB and CBTM is best at pH 3; hence, pH 3 is used for further study.

Influence of dosage on adsorption

The role of adsorbent dosage in the removal of rhodamine B by CBTM and CCB was systematically examined by varying the adsorbent mass from 0.01 g to 0.10 g, while maintaining constant solution concentration, pH, temperature, and other relevant adsorption conditions. As depicted in Figure 7, the percentage of RhB adsorbed onto both CBTM and CCB increased progressively with higher adsorbent doses. Specifically, as the adsorbent amount was raised from 0.01 g to 0.06 g, the RhB removal efficiency increased from 15% to 45% for CBTM and from 10% to 30% for CCB. The increase in the efficiency of the removal of rhodamine B by the

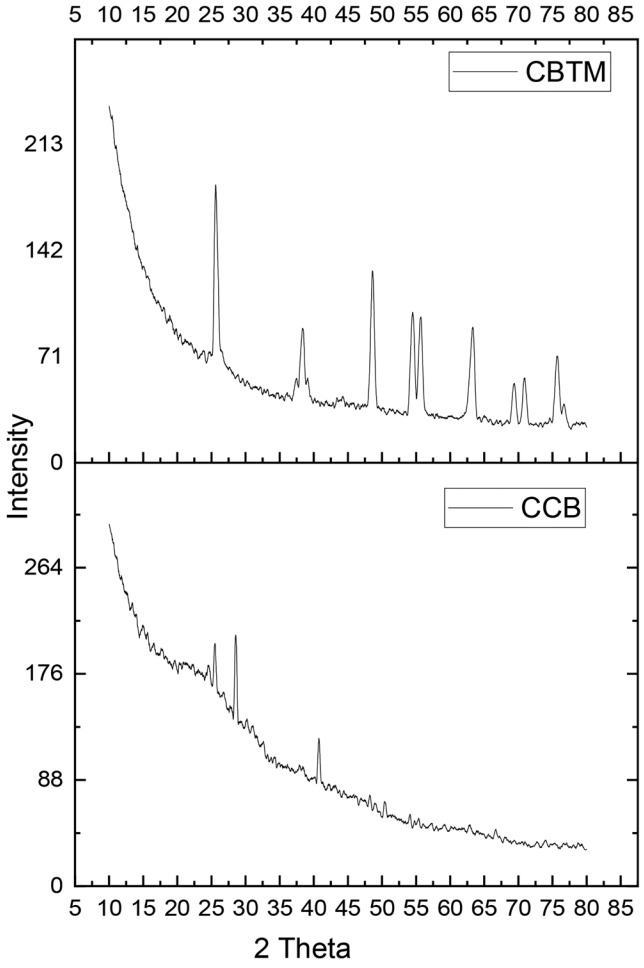

Figure 4. XRD pattern of CBTM and CCB.

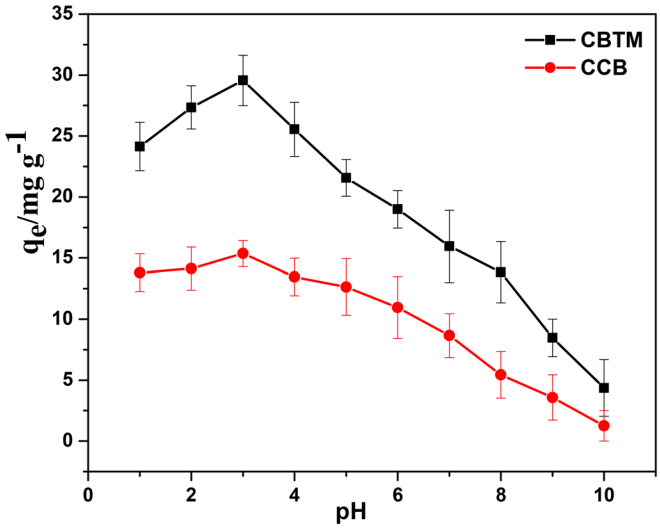

Figure 5. pHPZC plots of CBTM and CCB.

adsorbent is attributed to the increased number of available active sites and pores for sequestration of rhodamine B with increased dosage. On the other hand, the uptake potentials of CBTM and CCB were observed to decline with the increase in dosage; this could be due to increased agglomeration of the sorbent and the accumulation of unsaturated sites.

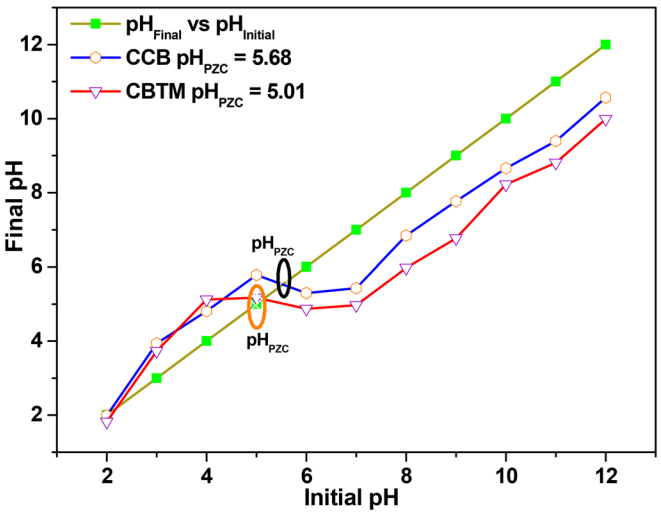

Figure 6. The influence of solution pH on the ability of CBTM and CCB to sequester RhB.

The effect of contact time

One crucial factor in comprehending the adsorption mechanism is the contact period between the adsorbent and adsorbate. The connection between adsorption capacity and contact time for both CBTM and CCB is shown in Figure 8. A 100 mg·L^{-1} RhB solution (25 cm^3) at 298 K and pH 3 was used for the investigation. An adsorbent dosage of 0.05 g and an agitation speed of 120 rpm were also used. From 0 to 180 min, the adsorption process was observed. A significant increase in RhB uptake was observed within the first 5 to 80 min for both materials, indicating rapid adsorption during the initial phase. Beyond 80 min, the rate of adsorption slowed noticeably, likely due to the saturation of available binding sites and pore spaces, suggesting that equilibrium had been reached. However, to ensure the saturation of the adsorbent surface, 180 min was employed for further studies.

Kinetics of the adsorption process

To elucidate the adsorption mechanism of rhodamine B onto CBTM and CCB, the uptake kinetics and rate-limiting steps were analyzed using four established models: pseudo-first-order (PFO), pseudo-second-order (PSO), Elovich, and intraparticle diffusion. Key kinetic parameters obtained from these models are summarized in Table 3 using the equation in Table 1. Nonlinear regression analysis was performed using the R statistical environment to ensure accurate model fitting. The sum of squared residuals (SSR) was employed as a quantitative measure of goodness-of-fit. Among the models evaluated, the one with the lowest SSR value was considered the most appropriate for describing the kinetic behavior. Based on this criterion, the PFO model was found to best characterize the adsorption of RhB onto both CBTM and CCB. Hence, it shows that the uptake of RhB onto CBTM and CCB followed a physisorptive process. This is in good agreement with the deduction made on the effect of the solution pH experiment. The intraparticle diffusion model (Wu *et al.* 2009) was applied to identify the rate-limiting step in the adsorption. It has been established that film or external diffusion, pore diffusion, or the

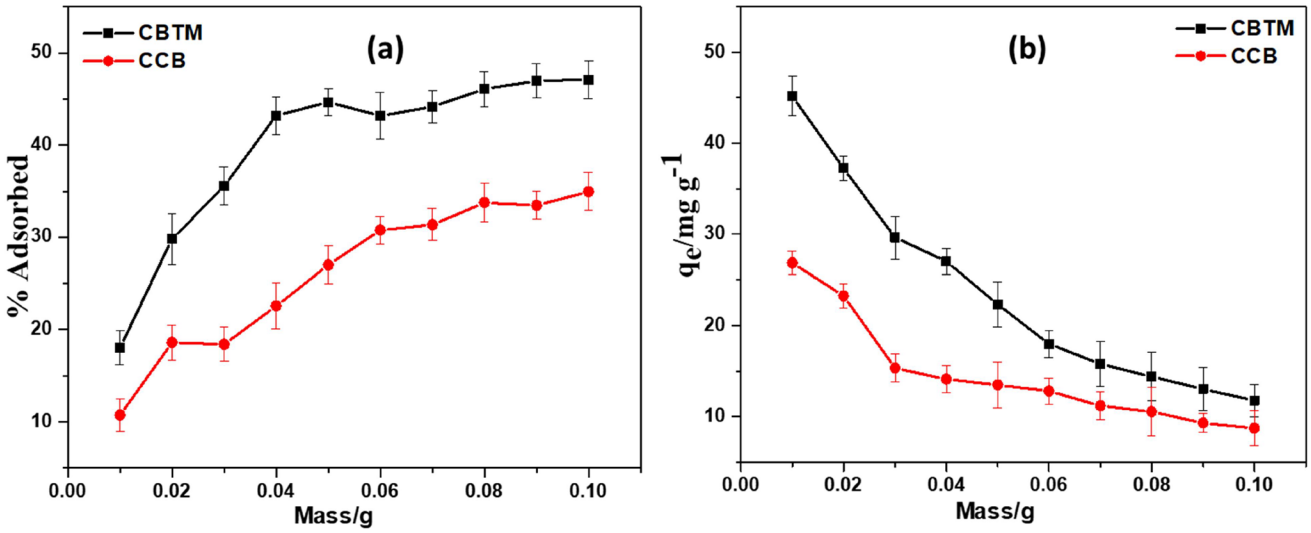

Figure 7. Variation of RhB adsorption with adsorbent dosage for CBTM and CCB: (a) % Adsorbed and (b) Adsorption Capacity.

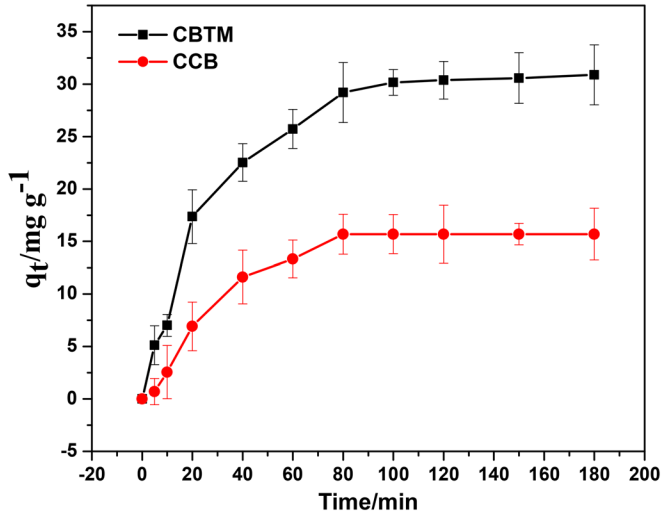

Figure 8. Contact time impact on RhB sequestration by CBTM and CCB.

Table 3. Kinetic parameters derived from RhB adsorption onto CBTM and CCB.

Model	Parameter	CBTM	CCB
experimental	q_{exp} (mg g^{-1})	32.45	16.89
Pseudo first order	K_1 (min^{-1})	0.03396	0.02776
	q_{eq} (mg g^{-1})	30.8632	16.39324
	SSR	9.881	6.249
	RSE	1.1111	0.8838
Pseudo-second order	K_2 (g $mg^{-1}min^{-1}$)	9.9×10-4	0.00131
	q_{eq} (mg g^{-1})	37.14	20.58927
	SSR	17.84	13.32
	RSE	1.495	1.290
Intraparticle diffusion	K_{id} (mg $g^{-1}min^{-0.5}$)	2.794	1.424
	I (mg g^{-1})	–	–
	SSR	148.1	47.92
	RSE	4.057	2.307
Elovich	α (mg $g^{-1}min^{-1}$)	−8.187	−6.989
	β (g mg^{-1})	8.038	4.744
	SSR	31.25	13.32
	RES	1.977	1.289

adsorption on the pore could be responsible for the rate-controlled step. In addition to the assertion, a combination of more than one step could also be responsible for the uptake of the adsorbate onto the adsorbent. To determine the rate-limiting step in the uptake process of RhB onto CBTM and CCB, a plot of qe vs $t^{0.5}$ was obtained. The linear plots revealed a nonzero intercept, and this indicates that the adsorption of RhB onto CBTM and CCB was controlled by a series of steps (Wang *et al.* 2024).

Adsorption isotherms

Figure 9 illustrates how variations in solution temperature and initial RhB concentration influence the adsorption performance of CBTM and CCB. The study employed an initial dye concentration range of 5–50 mg·dm^{-3}, while other experimental conditions were held constant. The tests were conducted at four different temperatures: 298, 303, 308, and 313 K. Results showed that the adsorption capacity of both CBTM and CCB increased with higher initial RhB concentrations, likely due to a steeper concentration gradient that enhances the diffusion of dye molecules into the adsorbent pores. A similar enhancement in uptake was observed with rising temperatures, which may be attributed to decreased solution viscosity, thereby facilitating faster molecular diffusion and improved access to active adsorption sites (Bello *et al.* 2020). To evaluate the interaction of RhB molecules with CBTM and CCB surfaces, equilibrium adsorption data were applied to two frequently used isotherm models, detailed in Table 2. The corresponding nonlinear isotherm curves were fitted and analyzed using the R statistical environment, and the extracted model parameters are summarized in Table 4. Based on the SSR values, the Freundlich model fitted the isotherm data obtained for CBTM and CCB. The fitting of isotherm data by the Freundlich model indicates that RhB adsorption by CBTM and CCB was a heterogeneous multilayer process. This heterogeneous nature of the adsorption is in good agreement with the porous, rough, and 2D structure of CBTM and CCB As shown in the SEM images in Figure 1, the dimensionless Freundlich constant (n) serves as an empirical indicator of the heterogeneity of adsorption sites present on the surface of the adsorbents.(Freundlich 1906). Additionally, the value of $1/n < 1$ (see Table 4) indicates favorable uptake of RhB onto

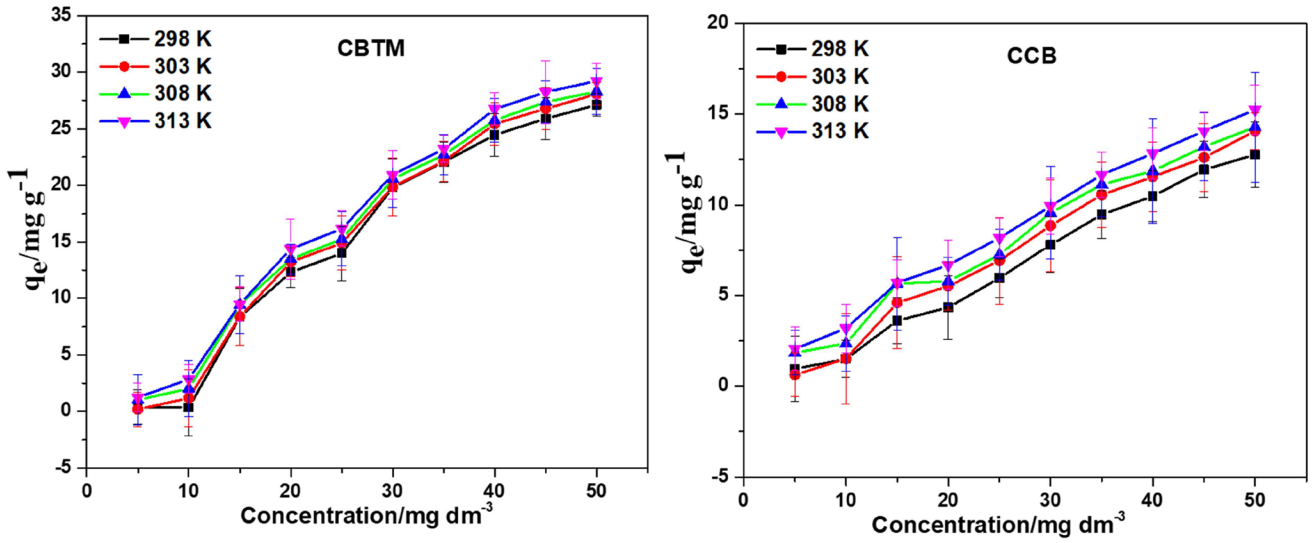

Figure 9. Impact of RhB Concentration on Uptake by (a) CBTM and (b) CCB at different temperatures.

Table 4. Parameters of Adsorption Isotherms for RhB Uptake on CBTM and CCB.

			Parameters	Temperature		
Adsorbent	Isotherm		298 K	303 K	308 K	313K
CBTM	Freundlich	K_F	1.2313	1.54916	2.8332	4.2330
		n	0.92169	0.96152	1.1556	1.33765
		SSR	213	277	415	467
	Langmuir	q_{max}	29.412	30.323	30.895	31.4325
		b	0.28429	0.2568	0.26785	0.2942
		SSR	589	278	414	465
CCB	Freundlich	K_F	0.13264	0.2567	0.65658	0.88984
		n	0.77075	0.87256	1.11895	1.2067
		SSR	5.617	8.1384	5.7818	1.7766
	Langmuir	q_{max}	15.4127	16.1353	16.8975	17.3211
		b	0.18429	0.2037	0.21037	0.2037
		SSR	2056	2268	5.9884	1.8073

Table 5. Comparison of the uptake potential of rhodamine B.

Adsorbent	Adsorption capacity/ mg g^{-1}	Reference
Fe-N-BC	12.41	(Li *et al.* 2022)
Acid-treated biomass	7.003	(Adekola *et al.* 2019)
Alkaline-treated biomass	6.878	(Adekola *et al.* 2019)
Alkaline-modified biochar	20.23	(Ibrahim *et al.* 2021)
CCB	17.32	This study
CBTM	31.43	This study

CBTM and CCB. However, the adaptability of the Freundlich model is significant at higher solution temperatures (308 and 313 K) as deduced from n values that are greater than 1. On the other hand, 17.26 and 31.25 mg g^{-1} maximum monolayer adsorption capacities were obtained at 313 K from the Langmuir model for CBTM and CCB, respectively. The removal capacity of CBTM was observed to be higher than CCB and other reported sorbent materials (see Table 5). An increase in solution temperature resulted in a linear rise in the uptake potential of both CBTM and CCB, suggesting that the adsorption of RhB onto these materials is an endothermic process. Previous studies on biochar-based materials have primarily focused on either adsorption performance or antimicrobial activity in isolation. In contrast, the present study integrates both functionalities by developing a multi-walled carbon nanotube/titanium dioxide ($MWCNT/TiO_2$)-modified biochar composite (CBTM), which simultaneously enhances Rhodamine B removal from wastewater and retains moderate antibacterial activity, highlighting its potential as a multifunctional material for wastewater treatment.

Adsorption thermodynamics

To gain deeper insight into the underlying mechanism of RhB removal from solution, temperature-dependent experimental data were analyzed to determine key thermodynamic parameters, including changes in Gibbs free energy (ΔG°), enthalpy (ΔH°), and entropy (ΔS°). These parameters were calculated using Equations 4 and 5.

$$\Delta G^\circ = -RT\ln K \tag{4}$$

$$\ln K = -\frac{\Delta H^\circ}{RT} + \frac{\Delta S^\circ}{R} \tag{5}$$

In this context, T represents the absolute temperature in Kelvin, R is the universal gas constant (8.314 J·mol^{-1}·K^{-1}), and K denotes a thermodynamic constant derived by multiplying the Langmuir constants q_{max} and b (expressed in dm^3·mol^{-1}), and scaling the result by 1000 to render it dimensionless (Milonjić 2007). The negative values of ΔG° obtained for both CBTM and CCB indicate that the adsorption of RhB onto these materials is thermodynamically favorable and occurs spontaneously (see Table 6). Meanwhile, the uptake of RhB onto CBTM and CCB was endothermic and was achieved at a higher degree of freedom. The acquired results are consistent with the report of other authors (Li *et al.* 2022; Amaku and Taziwa 2023).

Regeneration studies

An additional environmental issue arises when an adsorbent laden with RhB is disposed of, necessitating extra treatment. Consequently, it is important to regenerate adsorbent materials

by desorbing the dye. Desorption plays a crucial role in determining the degree of recovery of the adsorbed dye molecule from the surface of CBTM and CCB, as well as the subsequent reusability of these materials. Before reuse, RhB was desorbable from the surface of CBTM and CCB using 100% ethanol as an eluting agent. Figure 10 presents the findings. Following the fifth cycle, CBTM and CCB showed adsorption efficiencies of about 67% and 52%, respectively. In line with the results, ethanol demonstrated good efficiency for adsorbents' regeneration, and CBTM maintained its excellent ability to remove dyes from wastewater.

Antimicrobial and antioxidant activity

The result revealed that both materials show higher activity against *S. aureus* (Gram+) than *E. coli* (Gram–). However, CCB exhibits double the inhibition of CBTM for *S. aureus*, suggesting CCB has stronger antimicrobial properties (Table 7). The larger ZOI of the control confirms the validity of the assay and highlights that CCB and CBTM have moderate activity compared to clinical antibiotics. In contrast, the lower antimicrobial activity of CBTM relative to CCB may be due to surface modification altering the functional groups responsible for bacterial inhibition. In pristine biochar (CCB), oxygen-containing groups such as hydroxyl and carboxyl groups are abundant and can disrupt bacterial cell membranes or generate reactive oxygen species, contributing to higher antibacterial effects. The deposition of TiO_2 and MWCNTs in CBTM may partially block these functional groups or reduce their accessibility, thereby diminishing direct interactions with microbial cells. Consequently, while CBTM is optimized for adsorption efficiency, its antimicrobial activity is somewhat compromised compared to unmodified biochar. As a rapid, simple, and convenient method, the DPPH assay effectively assesses compound antioxidant activity. The antioxidant activity of the adsorbent materials is presented in Figure 11. The biochar CCB and nanocomposite CBTM possess mild radical scavenging activity as the concentration increases, although CBTM performs better than CCB. Ascorbic acid is used as the standard, while the DPPH solution is the control. It can be said that the CCB and CBTM, in addition to their capacity to adsorb pollutants, have considerable antioxidant and antibacterial capacity.

Table 6. Thermodynamic factors for absorption of RhB onto CBTM and CCB.

Adsorbents	T/K	ΔG°/kJ mol^{-1}	ΔH/ kJ mol^{-1}	ΔS/J K^{-1} mol^{-1}
CBTM	298	−22.3772	5.535	93.25
	303	−22.5733		
	310	−23.1015		
	318	−23.7656		
CCB	298	−19.5037		
	303	−20.5985	10.20	100.9
	310	−20.9377		
	318	−21.5977		

Table 7. Antimicrobial activity of CBTM and CCB against *Staphylococcus aureus* and *Escherichia coli*.

	Zone of inhibition (mm)	
Samples	*S. aureus*	*E.Coli*
CCB	8.0	1.3
CBTM	4.0	1.0
Control	20.0	15.0

Adsorption mechanism

The adsorption of Rhodamine B (RhB) onto CCB and CBTM is governed by a combination of physicochemical interactions, as supported by kinetic, isotherm, thermodynamic, and pH-dependent studies. The point of zero charge (pHPZC) values of CCB (5.68) and CBTM (5.01) indicate that at solution pH below these values, the surfaces are positively charged, while they become negatively charged at higher pH. Maximum adsorption occurred at pH 3, where RhB exists primarily as small monomeric cations that diffuse easily into the adsorbent pores and interact electrostatically with negatively charged functional groups. At higher pH values, RhB tends to form zwitterions and dimers, which, due to their larger size, experience steric hindrance and reduced pore accessibility, leading to a decline in adsorption capacity. Kinetic analysis showed that the process followed the pseudo-first-order model, confirming a physisorption-dominated mechanism, while intraparticle diffusion plots revealed that adsorption proceeded through multiple sequential steps involving both film diffusion and pore diffusion. The Freundlich isotherm provided the best fit to equilibrium data, suggesting multilayer adsorption on heterogeneous surfaces, consistent with SEM images that showed smooth, porous CCB surfaces and fibrous CNT networks in CBTM. Thermodynamic parameters further revealed that the adsorption was spontaneous (negative ΔG°), endothermic (positive ΔH°), and accompanied by increased interfacial randomness (positive ΔS°). The superior uptake capacity of CBTM compared to CCB is attributed to the synergistic effects of MWCNTs and TiO_2, which enhance surface heterogeneity, pore connectivity, and adsorption affinity through additional

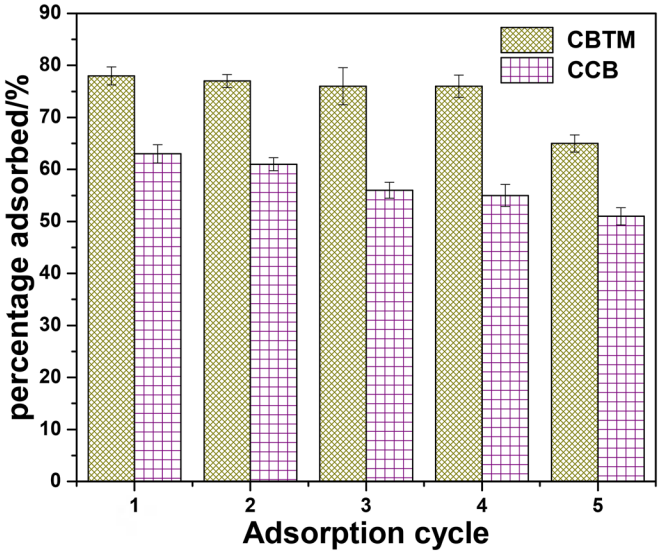

Figure 10. Reusability of CBTM and CCB for the uptake of RhB after ethanol washing (100 cm^3 of a 100 mg dm^{-3} of RhB solution adjusted to pH 6 and 30 mg of CBTM and CCB at 298 K).

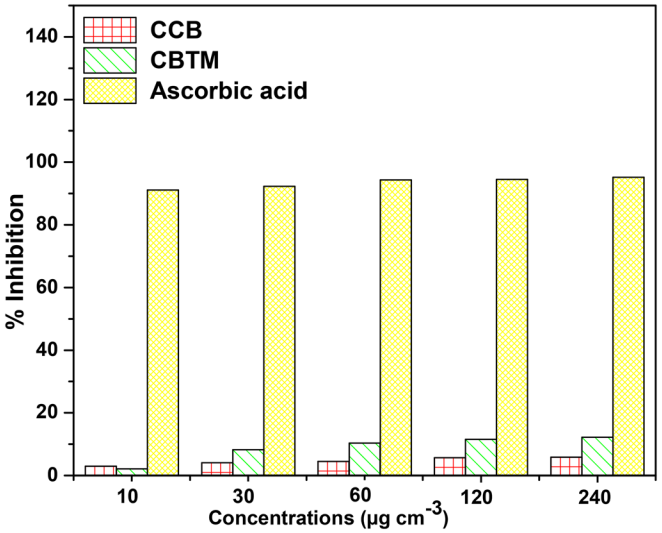

Figure 11. Percentage inhibition of CCB, CBTM, and ascorbic acid.

π–π stacking, hydrogen bonding, and electrostatic interactions. Overall, RhB adsorption onto CCB and CBTM is a physisorptive, diffusion-driven, multilayer process, with enhanced performance achieved through surface modification of biochar with TiO_2 and CNTs.

Conclusions

This study has demonstrated that a considerably more effective adsorbent for the removal of RhB was fabricated from the combination of MWCNTs/TiO_2 with biochar to create a composite. The uptake potential of the nanocomposite increased as the adsorbent dose, solution temperature, and RhB concentration increased, with the optimum adsorption taking place at pH 3. The adsorption equilibrium data for both CBTM and CCB were best interpreted using the Freundlich isotherm, indicating multilayer adsorption on heterogeneous surfaces. Langmuir analysis at 313 K revealed maximum adsorption capacities of 31.43 mg/g for the CBTM composite and 17.32 mg/g for CCB, suggesting a stronger affinity of RhB for the composite material. Rapid adsorption was observed for both materials, with equilibrium achieved within 180 min. Among the kinetic models evaluated, the pseudo-first-order model aligned most closely with the experimental data. Thermodynamic parameters confirmed that the adsorption process occurred spontaneously and was primarily influenced by an increase in system entropy. In addition to improving the adsorbent's dye-binding capabilities, the combination of MWCNTs and TiO_2 increases the mechanical robustness of the nanocomposite. As a result, the composite can be utilized in demanding industrial settings. All things considered, this composite is a desirable and prospective substitute for environmental contamination control, wastewater purification, and as an antioxidant.

Author contribution

James Friday Amaku: Conceptualization and Writing–original draft; **Ifeoma Anne Omobhude:** Writing – review & editing, Writing – original draft; **Okoche Kelvin Amadi:** Data curation, Conceptualization; **Tunde Lewis Yusuf:** Data curation, Editing; **Fanyana M. Mtunzi**: Supervision, Investigation, Writing – review & editing; **Jesse Greener;** Supervision, Investigation, Writing – review & editing.

Disclosure statement

The authors declare that they have no known competing financial interests or personal relationships that could have appeared to influence the work reported in this paper.

Funding

This work has received support from the South African National Research Foundation (NRF, grant numbers PSTD23040188896).

Data availability statement

The data that support the findings of this study are available from the corresponding author upon reasonable request.

References

Abu Hasan H, Muhammad MH, Ismail N. 2020. A review of biological drinking water treatment technologies for contaminants removal from polluted water resources. J Water Process Eng. 33:101035. doi:10.1016/j.jwpe.2019.101035.

Adekola FA, Ayodele SB, Inyinbor AA. 2019. Efficient rhodamine B removal using acidand alkaline-activated Musa paradisiaca biochar. Pol J Environ Stud. 28(5):3067–3070.

Adeogun AI, Balakrishnan RB. 2017. Kinetics, isothermal and thermodynamics studies of electrocoagulation removal of basic dye rhodamine B from aqueous solution using steel electrodes. Appl Water Sci. 7(4):1711–1723. doi:10.1007/s13201-015-0337-4.

Alsheheri SZ. 2021. Nanocomposites containing titanium dioxide for environmental remediation. Des Monomers Polym. 24(1):22–45. doi :10.1080/15685551.2021.1876322.

Al-Tohamy R, Ali SS, Li F, Okasha KM, Mahmoud YA-G, Elsamahy T, Jiao H, Fu Y, Sun J. 2022. A critical review on the treatment of dye-containing wastewater: ecotoxicological and health concerns of textile dyes and possible remediation approaches for environmental safety. Ecotoxicol Environ Saf. 231:113160. doi:10.1016/j.ecoenv.2021.113160.

Amaku JF, Taziwa R. 2023. Synthesis and characterization of nanocomposites containing Buchholzia coriacea pod decorated with multi-walled carbon nanotubes for remediation of rhodamine B dye from aqueous solution. Appl Water Sci. 13(12):228. doi:10.1007/s13201-023-02037-7.

Ambaye T, Vaccari M, van Hullebusch ED, Amrane A, Rtimi S. 2021. Mechanisms and adsorption capacities of biochar for the removal of organic and inorganic pollutants from industrial wastewater. Int J Environ Sci Technol. 18(10):3273–3294. doi:10.1007/s13762-020-03060-w.

Arun J, Nachiappan S, Rangarajan G, Alagappan RP, Gopinath K, Lichtfouse E. 2023. Synthesis and application of titanium dioxide photocatalysis for energy, decontamination and viral disinfection: a review. Environ Chem Lett. 21(1):339–362. doi:10.1007/s10311-022-01503-z.

Azam K, Shezad N, Shafiq I, Akhter P, Akhtar F, Jamil F, Shafique S, Park Y-K, Hussain M. 2022. A review on activated carbon modifications for the treatment of wastewater containing anionic dyes. Chemosphere. 306:135566. doi:10.1016/j.chemosphere.2022.135566.

Bella H, Bendaikha H. 2022. Biochar from empty date fruit bunch as an adsorbent to remove eriochrome black T and methylene blue from aqueous solution. App Envi Res. 44(2):44–55. doi:10.35762/AER.2022.44.2.4.

Bello OS, Alabi EO, Adegoke KA, Adegboyega SA, Inyinbor AA, Dada AO. 2020. Rhodamine B dye sequestration using Gmelina aborea leaf powder. Heliyon. 6(1):e02872. doi:10.1016/j.heliyon.2019.e02872.

Chougala L, Yatnatti M, Linganagoudar R, Kamble R, Kadadevarmath J. 2017. A simple approach on synthesis of TiO2 nanoparticles and its application in dye sensitized solar cells.

Chougala LS, Kadadevarmath JS, Kamble AA, Bayannavar PK, Yatnatti MS, Linganagoudar RK, Nirupama J, Kamble RR, Qiao Q. 2017. Effect of TiO2 nanoparticles on newly synthesized phenothiazine derivative-CPTA dye and its applications as dye sensitized solar cell. J Mol Liq. 244:97–102. doi:10.1016/j.molliq.2017.08.120.

Demiral İ, Samdan C, Demiral H. 2021. Enrichment of the surface functional groups of activated carbon by modification method. Surf Interfaces. 22:100873. doi:10.1016/j.surfin.2020.100873.

Deng C, Zhang G, Liu Y, Nie X, Li Z, Liu J, Zhu D. 2021. Advantages and disadvantages of terracing: a comprehensive review. Int Soil Water Conserv Res. 9(3):344–359. doi:10.1016/j.iswcr.2021.03.002.

Dutta P, Rabbi MR, Abu Sufian M, Mahjebin S. 2022. Effects of textile dyeing effluent on the environment and its treatment: a review. Eng. Appl. Sci. Lett. 5(1):1–1.

Elliott G, Mason R, Edwards I. 1990. Studies on the pharmacokinetics and mutagenic potential of rhodamine B. J Toxicol Clin Toxicol. 28(1):45–59. doi:10.3109/15563659008993475.

Feng D, Guo D, Zhang Y, Sun S, Zhao Y, Shang Q, Sun H, Wu J, Tan H. 2021. Functionalized construction of biochar with hierarchical pore structures and surface O-/N-containing groups for phenol adsorption. Chem Eng J. 410:127707. doi:10.1016/j.cej.2020.127707.

Firet NJ, Smith WA. 2017. Probing the reaction mechanism of CO2 electroreduction over Ag films via operando infrared spectroscopy. ACS Catal. 7(1):606–612. doi:10.1021/acscatal.6b02382.

Freundlich H. 1906. Freundlich's adsorption isotherm. Phys. Chem. 57:384.

Gkika DA, Mitropoulos AC, Kyzas GZ. 2022. Why reuse spent adsorbents? The latest challenges and limitations. Sci Total Environ. 822:153612. doi:10.1016/j.scitotenv.2022.153612.

Gupta A, Sharma R, Almond S. 2020. Antioxidants in vegetables and nuts-properties and health benefits. p. 423–452.

Gupta, V. K., Ali, Imran, Saini, V. K., Suhas,. 2004. Removal of rhodamine B, fast green, and methylene blue from wastewater using red mud, an aluminum industry waste. Ind Eng Chem Res. 43(7), 1740–1747. doi:10.1021/ie034218g.

Hayeeye F, Sattar M, Chinpa W, Sirichote O. 2017. Kinetics and thermodynamics of Rhodamine B adsorption by gelatin/activated carbon composite beads. Colloids Surf, A. 513:259–266. doi:10.1016/j.colsurfa.2016.10.052.

Ibrahim I, Batagarawa SB, Salisu A. 2021. Adsorption studies of rhodamine b dye from aqueous solution using alkaline modified biochar & non modified biochar obtained from the pyrolysis of municipal solid waste. FJS. 5(3):334–341. doi:10.33003/fjs-2021-0503-758.

Jafari M, Abbasi M, Enayati M, Karimzadeh F. 2012. Mechanical properties of nanostructured Al2024–MWCNT composite prepared by optimized mechanical milling and hot pressing methods. Adv Powder Technol. 23(2):205–210. doi:10.1016/j.apt.2011.02.008.

Jjagwe J, Olupot PW, Menya E, Kalibbala HM. 2021. Synthesis and application of granular activated carbon from biomass waste materials for water treatment: a review. J Bioresour Bioprod. 6(4):292–322. doi:10.1016/j.jobab.2021.03.003.

Khalid W, Afzal F, Jha RP, Afzal N, Khalid MZ, Shoaib T, Akram R, Gill P, Aziz A, Aslam N. 2021. Almond (Prunus dulcis): a nutritive dense dry fruit. Acta Sci Nutr Health. 5(7):38–46.

Khan MD, Singh A, Khan MZ, Tabraiz S, Sheikh J. 2023. Current perspectives, recent advancements, and efficiencies of various dye-containing wastewater treatment technologies. J Water Process Eng. 53:103579. doi:10.1016/j.jwpe.2023.103579.

Khan TA, Nazir M, Khan EA. 2013. Adsorptive removal of rhodamine B from textile wastewater using water chestnut (Trapa natans L.) peel: adsorption dynamics and kinetic studies. Toxicol Environ Chem. 95(6):919–931. doi:10.1080/02772248.2013.840369.

Krakowiak R, Musial J, Bakun P, Spychała M, Czarczynska-Goslinska B, Mlynarczyk DT, Koczorowski T, Sobotta L, Stanisz B, Goslinski T. 2021. Titanium dioxide-based photocatalysts for degradation of emerging contaminants including pharmaceutical pollutants. Appl Sci. 11(18):8674. doi:10.3390/app11188674.

Kumar, V. 2019. Adsorption kinetics and isotherms for the removal of rhodamine B dye and Pb+ 2 ions from aqueous solutions by a hybrid ion-exchanger. Arab J Chem, 12(3), 316–329. doi:10.1016/j.arabjc.2016.11.009.

Levent O. 2022. A detailed comparative study on some physicochemical properties, volatile composition, fatty acid, and mineral profile of different almond (Prunus dulcis L.) varieties. Horticulturae,. 8(6):488. doi:10.3390/horticulturae8060488.

Li X, Shi J, Luo X. 2022. Enhanced adsorption of rhodamine B from water by Fe-N co-modified biochar: preparation, performance, mechanism and reusability. Bioresour Technol. 343:126103. doi:10.1016/j.biortech.2021.126103.

Liu G, Zheng H, Jiang Z, Zhao J, Wang Z, Pan B, Xing B. 2018. Formation and physicochemical characteristics of nano biochar: insight into chemical and colloidal stability. Environ Sci Technol. 52(18):10369–10379. doi:10.1021/acs.est.8b01481.

Milonjić SK. 2007. A consideration of the correct calculation of thermodynamic parameters of adsorption. J Serb Chem Soc. 72(12):1363–1367.

Mondal NK, Basu S. 2019. Potentiality of waste human hair towards removal of chromium (VI) from solution: kinetic and equilibrium studies. Appl Water Sci. 9(3):49. doi:10.1007/s13201-019-0929-5.

Morin-Crini N, Lichtfouse E, Liu G, Balaram V, Ribeiro ARL, Lu Z, Stock F, Carmona E, Teixeira MR, Picos-Corrales LA. 2021. Emerging contaminants: analysis, aquatic compartments and water pollution. In Emerging contaminants Vol. 1: occurrence and impact. p. 1–111.

Morin-Crini N, Lichtfouse E, Liu G, Balaram V, Ribeiro ARL, Lu Z, Stock F, Carmona E, Teixeira MR, Picos-Corrales LA, *et al.* 2022. Worldwide cases of water pollution by emerging contaminants: a review. Environ Chem Lett. 20(4):2311–2338. doi:10.1007/s10311-022-01447-4.

Motahari F, Mozdianfard MR, Salavati-Niasari M. 2015. Synthesis and adsorption studies of NiO nanoparticles in the presence of H2acacen ligand, for removing Rhodamine B in wastewater treatment. Process Saf Environ Prot. 93:282–292. doi:10.1016/j.psep.2014.06.006.

Mousavi SA, Kamarehie B, Almasi A, Darvishmotevalli M, Salari M, Moradnia M, Azimi F, Ghaderpoori M, Neyazi Z, Karami MA. 2023. Removal of Rhodamine B from aqueous solution by stalk corn activated carbon: adsorption and kinetic study. Biomass Conv Bioref. 13(9):7927–7936. doi:10.1007/s13399-021-01628-1.

Parida VK, Saidulu D, Majumder A, Srivastava A, Gupta B, Gupta AK. 2021. Emerging contaminants in wastewater: a critical review on occurrence, existing legislations, risk assessment, and sustainable treatment alternatives. J Environ Chem Eng. 9(5):105966. doi:10.1016/j.jece.2021.105966.

Postai DL, Demarchi CA, Zanatta F, Melo DCC, Rodrigues CA. 2016. Adsorption of rhodamine B and methylene blue dyes using waste of seeds of Aleurites Moluccana, a low cost adsorbent. Alex Eng J. 55(2):1713–1723. doi:10.1016/j.aej.2016.03.017.

Qin F, Zhang C, Zeng G, Huang D, Tan X, Duan A. 2022. Lignocellulosic biomass carbonization for biochar production and characterization of biochar reactivity. Renewable Sustainable Energy Rev. 157:112056. doi:10.1016/j.rser.2021.112056.

Raguram T, Rajni K. 2022. Synthesis and characterisation of Cu-Doped TiO2 nanoparticles for DSSC and photocatalytic applications. Int J Hydrogen Energy. 47(7):4674–4689. doi:10.1016/j.ijhydene.2021.11.113.

Rajeev Jain RJ, Megha Mathur MM, Shalini Sikarwar SS, Alok Mittal AM. 2007. Removal of the hazardous dye rhodamine B through photocatalytic and adsorption treatments.

Ratanpara A, Kim M, Kim YJ, Hidrovo CH. 2025. Spectral characteristics of water-soluble rhodamine derivatives for laser-induced fluorescence. J Fluoresc. 35(6):4143–4155. doi:10.1007/s10895-024-03819-1.

Rathi BS, Kumar PS, Vo D-VN. 2021. Critical review on hazardous pollutants in water environment: occurrence, monitoring, fate, removal technologies and risk assessment. Sci Total Environ. 797:149134. doi:10.1016/j.scitotenv.2021.149134.

Rathi BS, Kumar PS. 2021. Application of adsorption process for effective removal of emerging contaminants from water and wastewater. Environ Pollut. 280:116995. doi:10.1016/j.envpol.2021.116995.

Reid AJ, Carlson AK, Creed IF, Eliason EJ, Gell PA, Johnson PTJ, Kidd KA, MacCormack TJ, Olden JD, Ormerod SJ, *et al.* 2019. Emerging threats and persistent conservation challenges for freshwater biodiversity. Biol Rev Camb Philos Soc. 94(3):849–873. doi:10.1111/brv.12480.

Saleh TA, Ali I. 2018. Synthesis of polyamide grafted carbon microspheres for removal of rhodamine B dye and heavy metals. J Environ Chem Eng. 6(4):5361–5368. doi:10.1016/j.jece.2018.08.033.

Saleh TA, Mustaqeem M, Khaled M. 2022. Water treatment technologies in removing heavy metal ions from wastewater: a review. Environ Nanotechnol Monit Manage. 17:100617. doi:10.1016/j.enmm.2021.100617.

Samsami S, Mohamadizaniani M, Sarrafzadeh M-H, Rene ER, Firoozbahr M. 2020. Recent advances in the treatment of dye-containing wastewater from textile industries: overview and perspectives. Process Saf Environ Prot. 143:138–163. doi:10.1016/j.psep.2020.05.034.

Saputro EA, Wulan VDR, Winata BY, Yogaswara RR, Erliyanti NK. 2020. Process of activated carbon form coconut shells through chemical activation. Nat Sci J. 9(1):23–28. 23—28. doi:10.22487/25411969.2020.v9.i1.15042.

Saravanan S, Carolin C F, Kumar PS, Chitra B, Rangasamy G. 2022. Biodegradation of textile dye Rhodamine-B by Brevundimonas diminuta and screening of their breakdown metabolites. Chemosphere. 308(Pt 1):136266. doi:10.1016/j.chemosphere.2022.136266.

Shabir M, Yasin M, Hussain M, Shafiq I, Akhter P, Nizami A-S, Jeon B-H, Park Y-K. 2022. A review on recent advances in the treatment of dye-polluted wastewater. J Ind Eng Chem. 112:1–19. doi:10.1016/j.jiec.2022.05.013.

Shah J, Rasul Jan M, Haq A, Khan Y. 2013. Removal of Rhodamine B from aqueous solutions and wastewater by walnut shells: kinetics, equilibrium and thermodynamics studies. Front Chem Sci Eng. 7(4):428–436. doi:10.1007/s11705-013-1358-x.

Shaikhiev IG, Kraysman NV, Sverguzova SV. 2021. Review of almond (Prunus dulcis) shell use to remove pollutants from aquatic environments. Biointerface Res Appl Chem. 11(6):14866–14880.

Sheng M-Q, Zhang W-W, Li H-J, Wu Y-C. 2024. Traditional and eco-friendly antiscalants: advantages and disadvantages. In: Ibrahim Yahia, Yaagoob and Chandrabhan Verma, editors. Industrial scale inhibition: principles, design, and applications. John Wiley & Sons, Inc. p. 18.

Smith B. 2017. The CO bond, Part I: introduction and the infrared spectroscopy of alcohols.

Vithalani PC, Bhatt NS. 2022. Degradation of rhodamine B, a xanthene dye by Aspergillus niger MSA2.

Waheed A, Baig N, Ullah N, Falath W. 2021. Removal of hazardous dyes, toxic metal ions and organic pollutants from wastewater by using porous hyper-cross-linked polymeric materials: a review of recent advances. J Environ Manage. 287:112360. doi:10.1016/j.jenvman.2021.112360.

Wang L, Shi C, Wang L, Pan L, Zhang X, Zou J-J. 2020. Rational design, synthesis, adsorption principles and applications of metal oxide adsorbents: a review. Nanoscale. 12(8):4790–4815. doi:10.1039/c9nr09274a.

Wang W, Guo J, Zhang Y, Shao L. 2024. Kinetic barrier networks: new insights on rate-limiting mechanisms in selective ion transport. Matter. 7(8):2671–2673. doi:10.1016/j.matt.2024.05.016.

Wu F-C, Tseng R-L, Juang R-S. 2009. Initial behavior of intraparticle diffusion model used in the description of adsorption kinetics. Chem Eng J. 153(1-3):1–8. doi:10.1016/j.cej.2009.04.042.

Wu J, Zhu K, Xu H, Yan W. 2019. Electrochemical oxidation of rhodamine B by PbO2/Sb-SnO2/TiO2 nanotube arrays electrode. Chin J Catal. 40(6):917–927. doi:10.1016/S1872-2067(19)63342-5.

Yan X, Tang W, Cui H. 2024. Effect of MWCNTs-OH on the mechanical properties of cement composites: from macro to micro perspective. Constr Build Mater. 444:137652. doi:10.1016/j.conbuildmat.2024.137652.

Yang Q, Ma Y, Chen F, Yao F, Sun J, Wang S, Yi K, Hou L, Li X, Wang D. 2019. Recent advances in photo-activated sulfate radical-advanced oxidation process (SR-AOP) for refractory organic pollutants removal in water. Chemical Engineering Journal. 378:122149. doi:10.1016/j.cej.2019.122149.

Yang W, Shang J, Li B, Flury M. 2020. Surface and colloid properties of biochar and implications for transport in porous media. Crit Rev Environ Sci Technol. 50(23):2484–2522. doi:10.1080/10643389.2019.1699381.

Yoo S, Kelley SS, Tilotta DC, Park S. 2018. Structural characterization of loblolly pine derived biochar by X-ray diffraction and electron energy loss spectroscopy. ACS Sustainable Chem Eng. 6(2):2621–2629. doi:10.1021/acssuschemeng.7b04119.